XL CILAMCE
IBERO-LATIN AMERICAN
CONGRESS ON
COMPUTATIONAL
METHODS IN
ENGINEERING

NOVEMBER
11-14, 2019
Praiamar Natal Hotel & Convention
Natal, RN-BRAZIL

EFFECTS OF DARCY AND REYNOLDS NUMBERS ON THE THERMAL BEHAVIOR OF A THERMOCLINE THERMAL STORAGE SYSTEM

Fernando A. Rodrigues
Marcelo J.S. de Lemos
ferar@ita.br
delemos@ita.br
Departamento de Energia - IEME
Instituto Tecnológico de Aeronáutica - ITA
12228-900 – São José dos Campos – S.P. Brazil

Abstract. This work explores the transient behavior of different flow velocities and porosities on the charging cycle of a thermocline thermal storage system for a concentrated solar power plant filled with solid porous material. In order to accomplish this goal, a transient model describing turbulent flow in a hybrid medium (porous/clear) with mixed convection was used. Macroscopic flow equations are obtained using the concept of double-decomposition. Discretization of the governing equations was performed with the SIMPLE method and the SIP procedure was used to relax the algebraic system of equations. Turbulent flow was modelled using the k-ε turbulence. A two-energy equation model was employed to assess heat transfer between solid and fluid phases. The analyzed geometry consists of an axisymmetrical tank with convection in the exterior, hot air flow entering the system from the top and clear regions at the top and bottom of the tank. Transient temperatures and storage and charge efficiencies were evaluated for different Da and Re number values. Results indicated that increasing Re values improve efficiency up to Re= 3.10^4 and further increases in Re slightly decreases thermal efficiencies. Finally, it was found that decreasing the permeability of the system by either lowering porosity or lowering particle diameter was beneficial for the thermal charge efficiency.

Keywords: Turbulent Flow, Thermal Non-Equilibrium, Porous Media, Ventilated cavity, Transient heat transfer

1 Introduction

Energy consumption on the interconnected Brazilian national grid is expected to grow 42% in the next 10 years, according to the Empresa de Pesquisa Energética [1] report from 2015. Following national and international tendencies it can be anticipated that some of this demand will be supplied by new renewable energy generation plants. Efficient renewable energy production systems must be developed to accomplish this goal and solar energy is amongst the most promising technology solutions to reduce environmental impact and fossil fuel consumption.

Solar energy generation is divided in two groups, solar photovoltaic (PV) and concentrated solar power (CSP). Solar PV directly converts solar energy into electricity using solar cells [2]. CSP systems use solar towers, parabolic troughs or Fresnel reflectors to concentrate solar energy and heat up a work fluid to high temperatures and then send it to a regular steam power plant [3]. CSP systems can be integrated with a thermal energy storage (TES) system and proceed to generate power during nighttime, which is an advantage over solar PV systems that still provide a technological challenge for efficient energy storage [4].

TES in CSP plants is paramount for the feasibility of this technology since it can shift energy production to peak demand times and through periods with intermittent cloud cover. Therefore, with the addition of a TES system CSP plants can continue to produce power even through periods without direct solar radiation [5].

This project focuses on the development and application of a model that simulate the thermal behavior of a reservoir for thermal energy storage filled with solid permeable material. The model will consider a turbulent flow in a hybrid medium (clear/porous), forced convection in a ventilated cavity with fluid inlet and outlet and natural convection due to buoyancy. The two-energy equation model will be used to evaluate heat transfer between the solid and fluid phases. Dynamic behavior of the system will be evaluated through the transient temperature variation. Turbulent flow and heat transfer in porous media will be modelled using the macroscopic two-energy equation model [6].

Previous work using these models was already published by the research group (LCFT/ITA) on turbulent flow in porous media [7] and hybrid media [8], with heat transfer due to forced convection [9] and natural convection [10], with extensive documentation in [11]. The present work will unite those models and add temporal variation while adding the specific application for TES systems.

2 Methodology

2.1 Problem description

The geometry of the thermocline tank is illustrated in Fig. 1. The tank has a d_t diameter of 5.0 m and a height H of 10 m, inlet and outlet both have a 0.5m diameter and the tank has a porous media of 8m in height. The working fluid is air and the solid is a porous ceramic material, whose property values are given in Table 1. The tank is axisymmetric with an initial temperature equilibrium of 200ºC and is subject to an inflow of hot air (550ºC) through the top port. A boundary condition of external convection with $h = 10W/m^2 - K$ and $T_\infty = 25^o C$ is considered for the tank side wall.

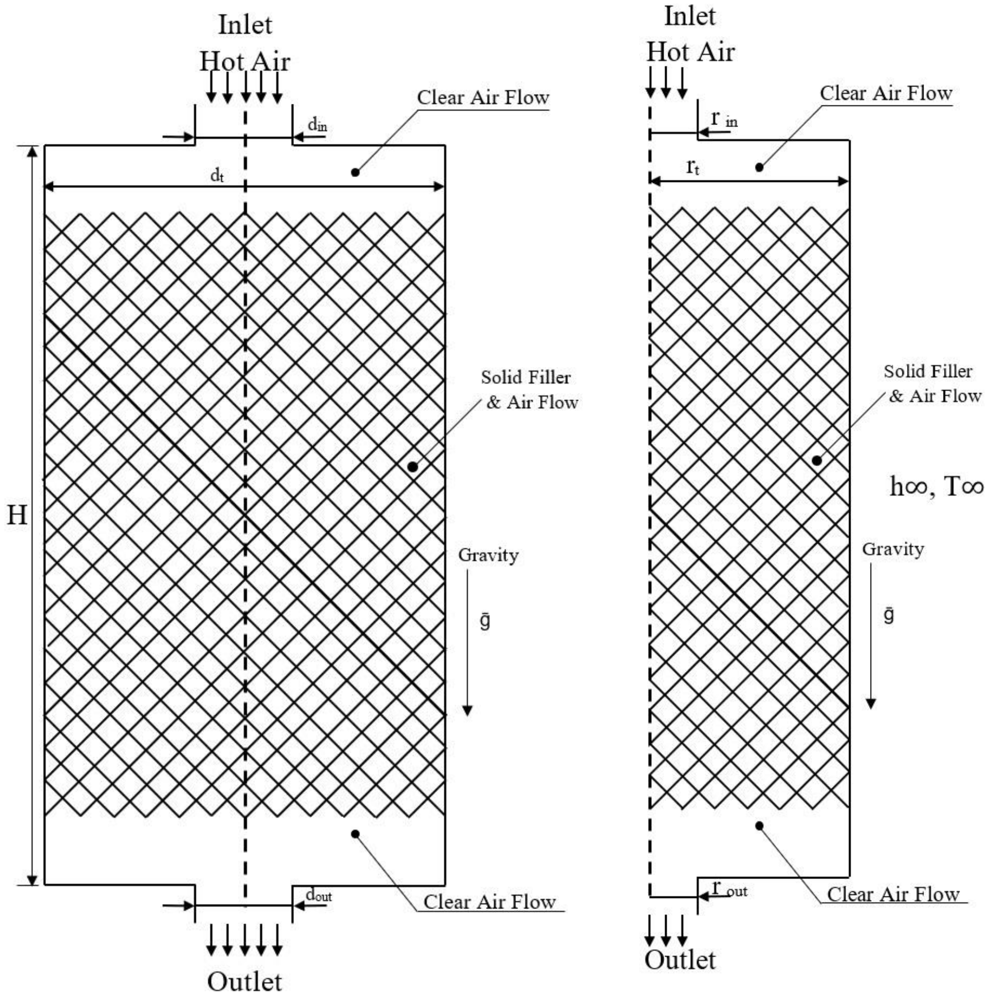

Figure 1 Geometry of the system under investigation.

Table 1. Material Properties employed

Property	Unit	Value
ρ_s	[kg/m^3]	830
c_{ps}	[kJ/kg-K]	2500
k_s	[W/m-K]	1.67
ρ_f	[kg/m^3]	0.596
c_{pf}	[kJ/kg-K]	1047
k_f	[W/m-K]	0.043
μ_f	[Ns/m^2]	29.3x10^{-6}
β_f	[1/K]	1.75x10^{-3}

2.2 Mathematical modeling

For an incompressible fluid the governing flow and energy equations are given by:
Continuity equation:

$$\nabla \cdot \mathbf{u} = 0 \tag{1}$$

Momentum Equation:

$$\rho\left[\frac{\partial \mathbf{u}}{\partial t} + \nabla \cdot (\mathbf{uu})\right] = -\nabla p + \mu \nabla^2 \mathbf{u} \tag{2}$$

Energy equation – Fluid Phase

$$(\rho c_p)_f \left[\frac{\partial T_f}{\partial t} + \nabla \cdot (\mathbf{u} T_f)\right] = \nabla.(k_f \nabla T_f) + S_f \tag{3}$$

Energy Equation – Solid Phase

$$(\rho c_p)_s \frac{\partial T_s}{\partial t} = \nabla.(k_s \nabla T_s) + S_s \tag{4}$$

where the subscripts s and f refer to the solid and fluid phase, respectively, T is the temperature, k is the thermal conductivity c_p is the specific heat and S is the heat generation term.

In the work developed in [12]–[14] the idea of double decomposition was introduced and described so that macroscopic transport equations which described turbulent flow in porous media could be obtained. The concept consists of a simultaneous application of time and volume averaged operators for a given property φ , the operators are:

$$\overline{\varphi} = \frac{1}{\Delta t}\int_t^{t+\Delta t} \varphi dt \ , \quad \text{with} \quad \varphi = \overline{\varphi} + \varphi' \tag{5}$$

$$\langle \varphi \rangle^i = \frac{1}{\Delta V_f} \int_{\Delta V_f} \varphi dV$$

$$\langle \varphi \rangle^v = \phi \langle \varphi \rangle^i$$

$$\phi = \frac{\Delta V_f}{\Delta V}, \qquad \text{with} \quad \varphi = \langle \varphi \rangle^i + {}^i\varphi \tag{6}$$

where ΔV_f is the fluid volume contained in a representative elementary volume (REV) ΔV , $\langle \varphi \rangle^i$ is the intrinsic average and $\langle \varphi \rangle^v$ is the volume average. Also, ${}^i\varphi$ is the spatial deviation of the property φ relative to the intrinsic average $\langle \varphi \rangle^i$.

Double decomposition consists of merging equations (5) and (6), by means of the following:

$$\overline{\langle \varphi \rangle^i} = \langle \overline{\varphi} \rangle^i \ ; \quad {}^i\overline{\varphi} = \overline{{}^i\varphi} \ ; \quad \langle \varphi' \rangle^i = \langle \varphi \rangle^{i'} \tag{7}$$

$$\left.\begin{aligned} \varphi' &= \langle \varphi' \rangle^i + {}^i\varphi' \\ {}^i\varphi &= \overline{{}^i\varphi} + {}^i\varphi' \end{aligned}\right\} \text{ where } \ {}^i\varphi' = \varphi' - \langle \varphi' \rangle^{i'} = {}^i\varphi - \overline{{}^i\varphi} \tag{8}$$

Thus, the given property φ can be represented by either (9) or (10):

$$\varphi = \overline{\langle \varphi \rangle^i} + \langle \varphi \rangle^{i'} + \overline{{}^i\varphi} + {}^i\varphi' \tag{9}$$

$$\varphi = \langle \overline{\varphi} \rangle^i + {}^i\overline{\varphi} + \langle \varphi' \rangle^i + {}^i\varphi' \tag{10}$$

where the term ${}^i\varphi'$ can be interpreted both as the time fluctuation of the spatial deviation and as the spatial deviation of the time fluctuation of the given property φ.

Using the double decomposition concept, the operators in (5) and (6) can be applied, simultaneously, in the governing equations (1) and (2) which yields macroscopic equations for turbulent flow. Subsequently, a volume integration over a REV is performed to obtain:

Continuity equation:

$$\nabla \cdot \bar{\mathbf{u}}_D = 0 \tag{11}$$

where $\bar{\mathbf{u}}_D$ is the average surface velocity, also known as Darcy's velocity. The Dupuit-Forchheimer relationship, $\mathbf{u}_D = \phi \langle \mathbf{u} \rangle^i$, is used in equation (11), where ϕ is the porosity of the porous medium and represents the intrinsic average of the local velocity vector **u**.[15]

Momentum Equation:

$$\begin{aligned} \rho\left[\frac{\partial \bar{\mathbf{u}}_D}{\partial t} + \nabla \cdot \left(\frac{\bar{\mathbf{u}}_D \bar{\mathbf{u}}_D}{\phi}\right)\right] &= -\nabla(\phi\langle \bar{p}\rangle^i) + \mu\nabla^2 \bar{\mathbf{u}}_D + \nabla \cdot (-\rho\phi\langle \overline{\mathbf{u}'\mathbf{u}'}\rangle^i) - \\ &- \rho\beta_\phi g\phi(\langle \overline{T_f}\rangle^i - T_{REF}) - \left[\frac{\mu\phi}{K}\bar{\mathbf{u}}_D + \frac{c_F \phi\rho |\bar{\mathbf{u}}_D|\, \bar{\mathbf{u}}_D}{\sqrt{K}}\right] \end{aligned} \tag{12}$$

where the term $-\rho\beta_\phi g\phi(\langle \overline{T_f}\rangle^i - T_{REF})$ represents natural convection and uses the intrinsic averaged temperature of the fluid. The last two terms of equation (12) represent the total drag forces modelled by the Darcy and Forchheimer term. letter K represents medium permeability and c_F is the Forchheimer coefficient.

The term $-\rho\phi\langle \overline{\mathbf{u}'\mathbf{u}'}\rangle^i$ is the macroscopic Reynolds stress and can be obtained by:

$$-\rho\phi\langle \overline{\mathbf{u}'\mathbf{u}'}\rangle^i = \mu_{t_\phi} 2\langle \bar{\mathbf{D}}\rangle^{\mathrm{v}} - \frac{2}{3}\phi\rho\langle k\rangle^i \mathbf{I} \tag{13}$$

where

$$\langle \bar{\mathbf{D}}\rangle^v = \frac{1}{2}\left[\nabla(\phi\langle \bar{\mathbf{u}}\rangle^i) + [\nabla(\phi\langle \bar{\mathbf{u}}\rangle^i)]^T\right] \tag{14}$$

represents the macroscopic deformation tensor, **I** is the unit tensor and μ_{t_ϕ} is the turbulent viscosity, which is modelled as:

$$\mu_{t_\phi} = \rho c_\mu \frac{\langle k\rangle^{i\,2}}{\langle \varepsilon\rangle^i} \tag{15}$$

where c_μ is a non-dimensional empirical constant. Hence, $\langle k\rangle^i$ and $\langle \varepsilon\rangle^i$ must be obtained through the transport equations in order to get μ_{t_ϕ}.

The macroscopic turbulent kinetic energy equation is:

$$\rho\left[\frac{\partial}{\partial t}(\phi\langle k\rangle^{i})+\nabla\cdot(\overline{\mathbf{u}}_{D}\langle k\rangle^{i})\right]=\nabla\cdot\left[(\mu+\frac{\mu_{t_\phi}}{\sigma_k})\nabla(\phi\langle k\rangle^{i})\right]- \\ -\rho\langle\overline{\mathbf{u}'\mathbf{u}'}\rangle^{i}\nabla\overline{\mathbf{u}}_{D}+C_k\rho\frac{\phi k_\phi|\overline{\mathbf{u}}_D|}{\sqrt{K}}+G_\beta^i-\rho\phi\langle\varepsilon\rangle^{i} \tag{16}$$

where $\rho\langle\overline{\mathbf{u}'\mathbf{u}'}\rangle^{i}$ is defined by equation (13) and σ_k is a non-dimensional empirical constant. The term $G_\beta^i=\phi\frac{\mu_{t_\phi}}{\sigma_t}\beta_\phi^k\mathbf{g}\cdot\nabla\langle\overline{T}\rangle^{i}$ represents the generation of $\langle k\rangle^{i}$ due to natural convection, where $\beta_\phi=\frac{\langle\rho\beta(T-T_{ref})\rangle^{v}}{\rho\phi(\langle T\rangle^{i}-T_{ref})}$ is the macroscopic thermal expansion coefficient and $\beta_\phi^k=\frac{\langle\beta\overline{\mathbf{u}'T'}\rangle^{v}}{\phi(\overline{\mathbf{u}'T_f'})}$ is the macroscopic thermal coefficient.

The macroscopic turbulent kinetic energy dissipation equation is:

$$\rho\left[\frac{\partial}{\partial t}(\phi\langle\varepsilon\rangle^{i})+\nabla\cdot(\overline{\mathbf{u}}_{D}\langle\varepsilon\rangle^{i})\right]=\nabla\cdot\left[(\mu+\frac{\mu_{t_\phi}}{\sigma_\varepsilon})\nabla(\phi\langle\varepsilon\rangle^{i})\right]+ \\ +c_1(-\rho\langle\overline{\mathbf{u}'\mathbf{u}'}\rangle^{i}\nabla\overline{\mathbf{u}}_{D})\frac{\langle\varepsilon\rangle^{i}}{\langle k\rangle^{i}}+c_2C_k\rho\frac{\phi\varepsilon_\phi|\overline{\mathbf{u}}_D|}{\sqrt{K}}+c_1c_3G_\beta^i\frac{\langle\varepsilon\rangle^{i}}{\langle k\rangle^{i}}-c_2\rho\phi\frac{\langle\varepsilon\rangle^{i\,2}}{\langle k\rangle^{i}} \tag{17}$$

where σ_ε, c_1, c_2 and c_3 are non-dimensional empirical constants

Using the time and volume average operators, described beforehand in equations (5) and (6), the macroscopic energy equations for the solid and fluid phase are obtained. After performing a volume integration over a REV the resulting equations are:

For the fluid phase

$$(\rho c_p)_f\left[\frac{\partial\phi\langle\overline{T}_f\rangle^{i}}{\partial t}+\nabla\cdot\left\{\phi\left(\langle\overline{\mathbf{u}}\rangle^{i}\langle\overline{T}_f\rangle^{i}+\langle{}^{i}\overline{\mathbf{u}}{}^{i}\overline{T}_f\rangle^{i}+\overline{\langle\mathbf{u}'\rangle^{i}\langle T_f'\rangle^{i}}+\langle\overline{{}^{i}\mathbf{u}'{}^{i}T_f'}\rangle^{i}\right)\right\}\right]= \\ =\nabla.\left[k_f\nabla\left(\phi\langle\overline{T}_f\rangle^{i}\right)+\frac{1}{\Delta V}\int_{A_i}\mathbf{n}_i\,k_f\,\overline{T_f}\,dA\right]+\frac{1}{\Delta V}\int_{A_i}\mathbf{n}_i\,k_f\,\overline{T_f}\,dA \tag{18}$$

And for the solid phase:

$$(\rho c_p)_s\left\{\frac{\partial(1-\phi)\langle\overline{T}_s\rangle^{i}}{\partial t}\right\}=\nabla.\left\{k_s\nabla\left[(1-\phi)\langle\overline{T}_s\rangle^{i}\right]-\frac{1}{\Delta V}\int_{A_i}\mathbf{n}_i\,k_s\overline{T}_s\,dA\right\}-\frac{1}{\Delta V}\int_{A_i}\mathbf{n}_i\,k_s\overline{T}_s\,dA \tag{19}$$

where A_i is the interfacial area inside the REV and $\mathbf{n}_i$ is the unit vector normal to the fluid-solid interface, pointing from the fluid to the solid phase. The intrinsic average temperatures of the solid and fluid phase, $\langle\overline{T}_s\rangle^{i}$ and $\langle\overline{T}_f\rangle^{i}$, need to be modelled to utilize equations (18) and (19).

For equation (18), the term $\langle{}^{i}\overline{\mathbf{u}}{}^{i}\overline{T}_f\rangle^{i}$ represents the thermal dispersion, $\overline{\langle\mathbf{u}'\rangle^{i}\langle T_f'\rangle^{i}}$ represents turbulent heat flow and $\langle\overline{{}^{i}\mathbf{u}'{}^{i}T_f'}\rangle^{i}$ turbulent thermal dispersion. These terms can be modelled using the following equations:

Thermal dispersion:

$$-\left(\rho c_p\right)_f \left(\phi \; \langle {}^i\bar{\mathbf{u}}\, \overline{{}^iT_f}\rangle^i \right) = \mathbf{K}_{disp} \cdot \nabla \langle \overline{T}_f \rangle^i \tag{20}$$

Turbulent heat flow

$$-\left(\rho\, c_p\right)_f \left(\phi \; \overline{\langle \mathbf{u}' \rangle^i \langle T_f' \rangle^i} \right) = \mathbf{K}_t \cdot \nabla \langle \overline{T}_f \rangle^i \tag{21}$$

Turbulent thermal dispersion:

$$-\left(\rho c_p\right)_f \left(\phi \; \langle \overline{{}^i\mathbf{u}' \; {}^iT_f'} \rangle^i \right) = \mathbf{K}_{disp,t} \cdot \nabla \langle \overline{T}_f \rangle^i \tag{22}$$

where $\mathbf{K}_{disp}$ $\mathbf{K}_t$, and $\mathbf{K}_{disp,t}$ are, respectively, the thermal dispersion tensor, turbulent heat flow tensor and turbulent thermal dispersion tensor.

For both (18) and (19) equations the two terms on the right-hand side represent conduction and interfacial heat transfer, respectively. The conduction terms can be expressed by the following relationship:

$$\nabla . \left[\frac{1}{\Delta V} \int_{A_i} \mathbf{n}_i \, k_f \, \overline{T_f} \; dA \right] = \mathbf{K}_{f,s} \cdot \nabla \langle \overline{T}_s \rangle^i - \nabla . \left[\frac{1}{\Delta V} \int_{A_i} \mathbf{n}_i \, k_s \overline{T_s} \; dA \right] = \mathbf{K}_{s,f} \cdot \nabla \langle \overline{T}_f \rangle^i \tag{23}$$

where $\mathbf{K}_{f,s}$ and $\mathbf{K}_{s,f}$ are the local conduction tensors between fluid and solid.

The tensors $\mathbf{K}_{disp}$, $\mathbf{K}_t$, $\mathbf{K}_{disp,t}$, $\mathbf{K}_{f,s}$ and $\mathbf{K}_{s,f}$ are denominated thermal conductivity tensors and can be associated by means of an effective thermal conductivity tensor for both the fluid ($\mathbf{K}_{eff,f}$) and the solid phase ($\mathbf{K}_{eff,s}$), as:

$$\mathbf{K}_{eff,f} = [\phi k_f] \, \mathbf{I} + \mathbf{K}_{f,s} + \mathbf{K}_{disp} + \mathbf{K}_{disp,t} + \mathbf{K}_t \tag{24}$$

$$\mathbf{K}_{eff,s} = [(1-\phi) k_s] \, \mathbf{I} + \mathbf{K}_{s,f} \tag{25}$$

where **I** is the unity tensor.

Interfacial heat transfer is represented by the last term on the right-hand side of equations (18) and (19) and can be modelled through a film coefficient h_i so that:

$$h_i a_i \left(\langle \overline{T_s} \rangle^i - \langle \overline{T_f} \rangle^i \right) = \frac{1}{\Delta V} \int_{A_i} \mathbf{n}_i \cdot k_f \nabla \overline{T_f} \; dA = \frac{1}{\Delta V} \int_{A_i} \mathbf{n}_i \cdot k_s \nabla \overline{T_s} \; dA \tag{26}$$

where $a_i = A_i / \Delta V$ is the superficial area per unit volume.

Finally, merging the terms in the macroscopic energy equations (fluid phase (18) and solid phase (19)) with equations (20), (21), (22), (23), (24), (25) and (26), an energy balance for each phase is obtained as:

$$\left\{ (\rho c_p)_f \, \phi \right\} \frac{\partial \left\langle \overline{T}_f \right\rangle^i}{\partial t} + (\rho c_p)_f \, \nabla . \left(\mathbf{u}_D \left\langle \overline{T}_f \right\rangle^i \right) = \nabla . \left\{ \mathbf{K}_{eff,f} \nabla \left\langle \overline{T}_f \right\rangle^i \right\} + h_i a_i \left(\langle \overline{T_s} \rangle^i - \langle \overline{T_f} \rangle^i \right) \tag{27}$$

$$\left\{ (1-\phi)(\rho c_p)_s \right\} \frac{\partial \left\langle \overline{T}_s \right\rangle^i}{\partial t} = \nabla . \left\{ \mathbf{K}_{eff,s} \nabla \left\langle \overline{T}_s \right\rangle^i \right\} - h_i a_i \left(\langle \overline{T_s} \rangle^i - \langle \overline{T_f} \rangle^i \right) \qquad (28$$

2.3 Numerical Method

Finite volume method [16] with a collocated grid will be used for the discretization of the equations. SIMPLE algorithm will be used to correct the pressure field (to avoid issues with pressure field oscillations the velocities are obtained by individual interpolation, using discretized momentum equations on the nodes and the pressure differences across the faces are evaluated as in staggered grids). A hybrid interpolation scheme (Upwind (UDS) and central differences (CDS)) will be used for the convective terms. The implicit method will be used to evaluate the transient behavior of the system, with the equations being solved for both the present state t and the following state $t+\Delta t$.

2.4 Evaluated parameters

Several parameters are used to evaluate different aspects of the system's behavior. An average Nusselt number was calculated along the side wall of the tank. Since a Two-Energy Equation model is used in the model the local Nusselt number is given by,

$$Nu_{w_y} = -\frac{(q_f + q_s)}{k_{eff}} \frac{H}{T_H - T_C} \tag{29}$$

where q_f and q_s are the heat fluxes for each of the phases.

The local Nu_y can then be integrated over the tank wall length H, yielding an average Nu_w number.

$$Nu_w = \frac{1}{H}\int_0^H Nu_{w_y}\, dy \tag{30}$$

Darcy number is evaluated using the permeability K and the height of the cavity H as:

$$Da = \frac{K}{H^2} \tag{31}$$

where the permeability is found using Ergun's equation with the particle diameter d_p: and the porosity ϕ, as:

$$K = \frac{{d_p}^2 \phi^3}{144(1-\phi)^2} \tag{32}$$

The efficiency in which the system stores energy (η_{st}) can be evaluated as:

$$\eta_{st}(t^*) = \frac{E_{St}(t^*)}{E_{In}(t^*)} \tag{33}$$

where

$$E_{St} = \frac{(1-\phi)\rho_s c_{ps}}{V_S} \int_0^{V_S} [T_S(t^*) - T_{in}]\, dV_S \tag{34}$$

and

$$E_{in} = c_{pf}\,\rho_f\, u \pi {r_{in}}^2 \int_0^{t^*} (T_{in} - T_0)\, dt \tag{35}$$

Physically, Eq. (33) is the ratio between the energy that is stored by the solid phase (E_{St}) and the energy that enters the system (E_{in}) at each instant in time t^*.

Furthermore, the total charge efficiency (η_{chg}) can be taken as

$$\eta_{chg}(t^*) = \frac{E_{St}(t^*)}{E_{Max}} \tag{36}$$

where

$$E_{Max} = (1-\phi)\rho_s c_{ps} V_S \left(T_{in} - T_0\right) \tag{37}$$

Here, eq. (36) is the ratio between the total stored energy in the solid phase (E_{St}) and the maximum theoretical energy that can be stored by the solid (E_{Max}).

3 Results and Discussion

3.1 Grid size independency

Eight grids varying from 3000 to 23980 elements were used to assess the solution's independence relative to the size of the grid. Values for Nu_w and E_{St} were compared for these grids and it was found that after 19800 elements further grid refinement did not influence the result. However, the grid of choice for the cases in this work had 12640 elements (79x160), since it diminished significantly the computational cost while its results were negligibly different (Nu_w varying 0.2% and E_{St} 0.1%) than more refined grids. The convergence criterion for all variables was set to 10^{-4}.

3.2 Model Validation

Validation of the thermal behavior of the solution was performed using the measurements taken in [17], where a thermal storage tank with a packed pebble bed was heated up using heat transfer oil. Figure 2a illustrates the comparison between simulated and experimental temperatures along the tank during the charge. Each of the curves represent the transient temperature at a given depth of the tank. Despite simulation results yielding values close to those of the experiment there is a small difference in some curves. The difference is probably due to the changing properties in the experiment with respect to temperature while the numerical model uses an average value, particularly concerning the change in viscosity for the heat transfer oil used. To show that, Figure 2b presents the variation of viscosity with regards to temperature in the experiment and the value used in the model.

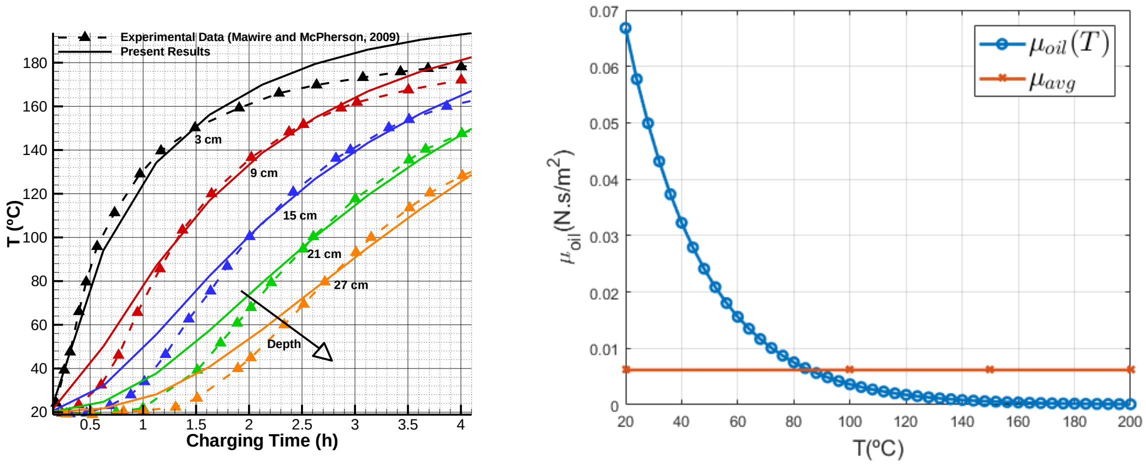

(a) (b)

Figure 2. Thermal behavior validation: (a) Comparison between transient temperature at different tank depths obtained experimentally [17] and those from present simulations. (b) Variation of viscosity with temperature from the heat exchange oil used in the experimental work and averaged viscosity used in the simulations.

3.3 Transient temperatures

The use of the thermal non-equilibrium model has the benefit of providing independent temperatures for solid and fluid phases throughout the charging cycle. Figure 3a portrays the two-dimensional temperature maps for the temperature distribution of the fluid in the tank whereas Figure 3b shows the temperature distribution for the solid phase. Hydrodynamic properties for the calculations in the figure where Re=30000, $d_p=1.10^{-1}$ m and $\phi=0.8$. Due to the outside convection boundary condition (see Fig. 1), a thin temperature boundary layer forms close to the internal tank wall. From these plots, the difference between the evolution in time of the temperatures in the solid and fluid phases can be seen.

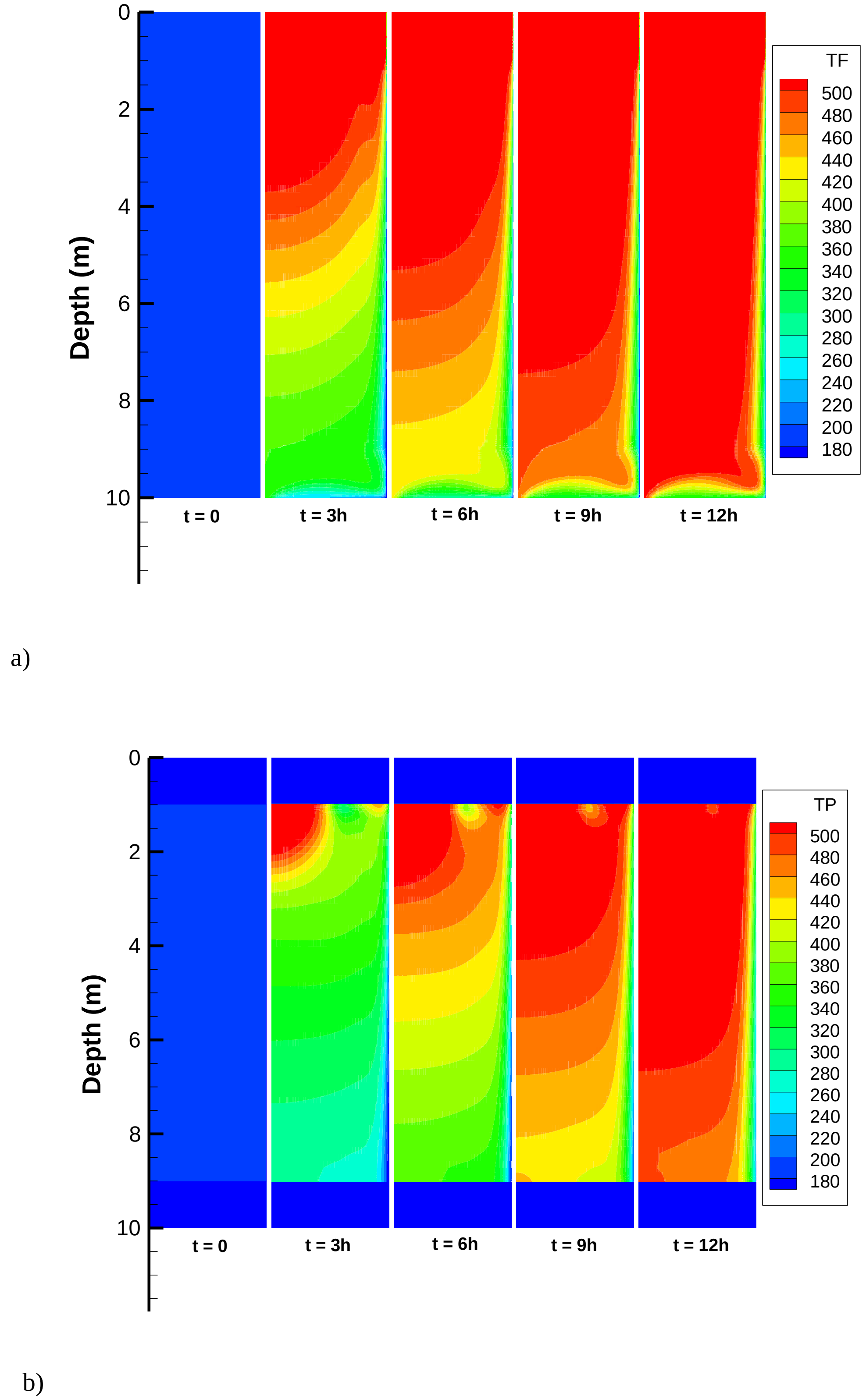

Figure 3. Two-dimensional temperature maps for $d_p = 1.10^{-1} m$ and $\phi = 0.80$: (a) Fluid temperature, T_f; (b) Solid temperature, T_s.

This difference is diminished when the particle diameter is changed to d_p=1.10^{-3} m as illustrated by Figure 4, where not only the temperatures are closer to each other for both phases but the total heating of the solid phase occurs much sooner, at t=9h. By reducing d_p, the interstitial heat transfer area increases for the same porosity, enhancing heat exchange between phases.

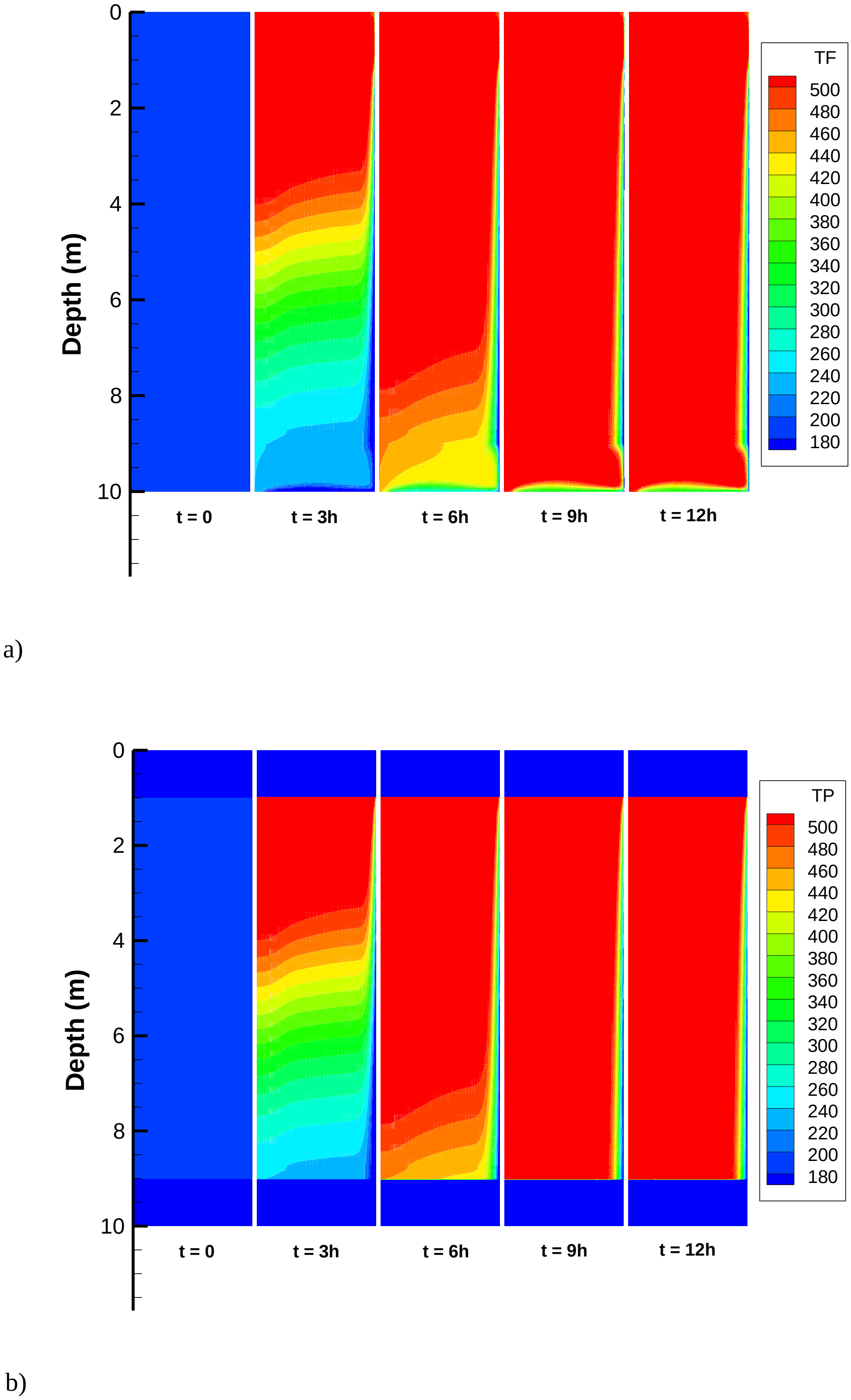

Figure 4. Two-dimensional temperature maps for $d_p = 1.10^{-3} m$ and $\phi = 0.80$: (a) Fluid temperature, T_f; (b) Solid temperature, T_s.

Figure 5a shows the transient solid and fluid temperatures at the mid-height of the tank for three different porosities, namely, 0.8, 0.85 and 0.9. Difference in porosities do not affect substantially the differences between solid and fluid temperatures. However, lower porosities imply in more material causing fluid temperatures to rise slower. By that, the fluid phase loses more momentum causing its temperature to rise later during the charge.

Opposingly, changes in particle diameter substantially affect heat transfer between both phases. Figure 5b shows the transient solid and fluid temperatures at the mid-point of the tank for particle diameters of d_p=1.10^{-1} m, 1.10^{-2} m and 1.10^{-3} m. From the figure, smaller particles effect smaller differences in temperature amongst the two phases. This result is due to the increase in the heat exchange area between phases with decreasing radius. It is also notable that, with larger particles, the fluid phase has a higher temperature in the first time steps of the charge due to eased fluid flow through the porous medium.

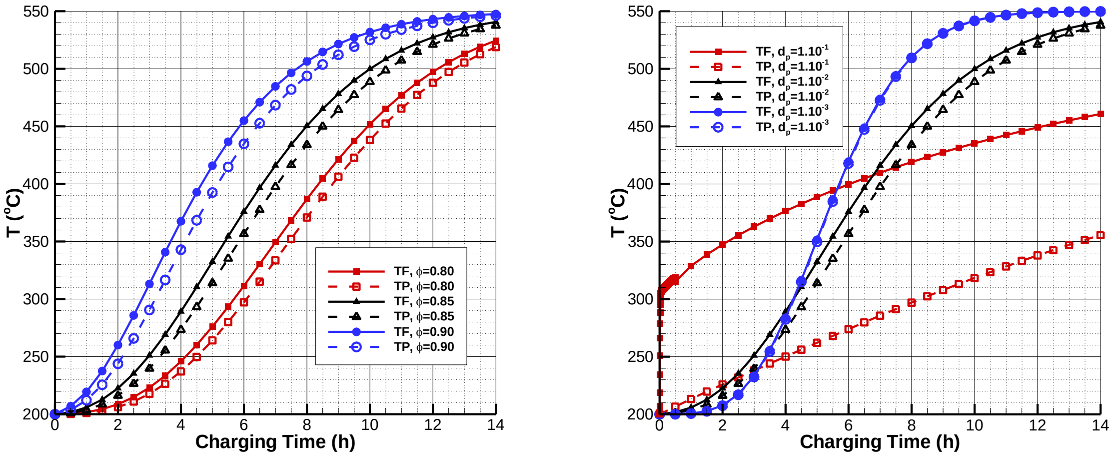

a) b)

Figure 5. Transient fluid and solid temperatures at the tank mid-height (r=0, z=H/2) for Re=1.10^4: (a) varying porosities, ϕ; (b) varying particle diameters, d_p.

3.4 Efficiencies, η

To evaluate the charge, the efficiency in which the porous matrix stores heat (η_{st}) was plotted alongside the percentage of the theoretical total energy that can be stored in the tank by the porous material (η_{chg}). Equations for η_{st} and η_{chg} were defined in eq. (33) and (36), respectively. Figure 6 portrays the efficiencies for different porosities and Re values for Re=1.10^4 and Re=6.10^4. Lower porosities translate into a slower charge due to the increased amount of solid material, but the storage efficiency is higher than that of higher porosities. Higher porosities present a less efficient absorption of the inlet thermal energy due to decreased contact between the solid and fluid phases and hence decreased heat exchange. Not unexpectedly, decreasing Re values effect significant increases in charging time, but also translate into smoother drops in storage efficiency due to hot fluid leaving the tank more slowly.

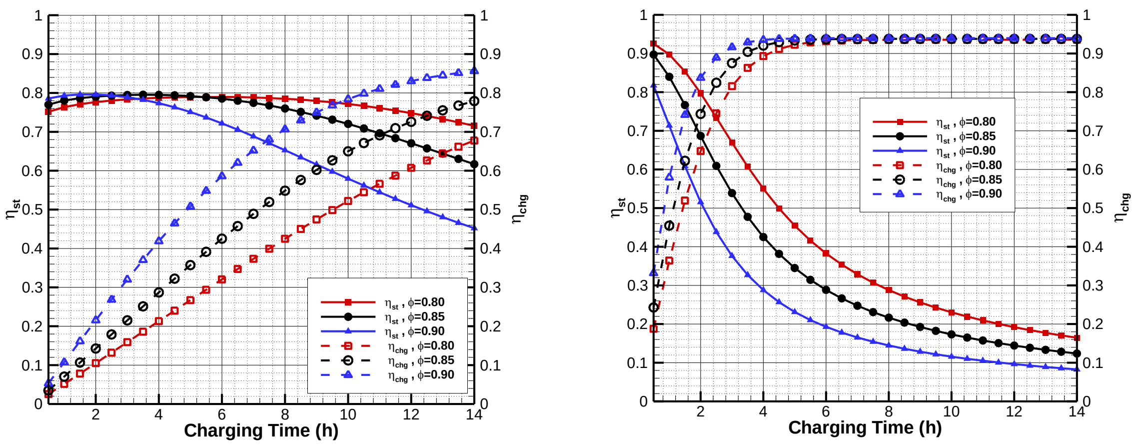

a) b)

Figure 6. Charge and storage efficiencies during the charge with different porosities, for: a)Re=1.10^4 b)Re=6.10^4

The efficiencies were also examined for different particle diameters in Figure 7. As before, smaller particle diameters perform better due to the increased heat exchange between the solid and fluid phases making it so that less hot fluid leaves the tank without giving out heat. The diminished heat exchange for bigger particles translate into slower charges with lower storage efficiencies. However, the variance between particles with $d_p=1.10^{-2}$ m and $d_p=1.10^{-3}$ m is very small, implying that the enhancement in the heat storage efficiency is already close to the maximum at $d_p=1.10^{-2}$ m and from there is a significant decrease when $d_p=1.10^{-1}$ m.

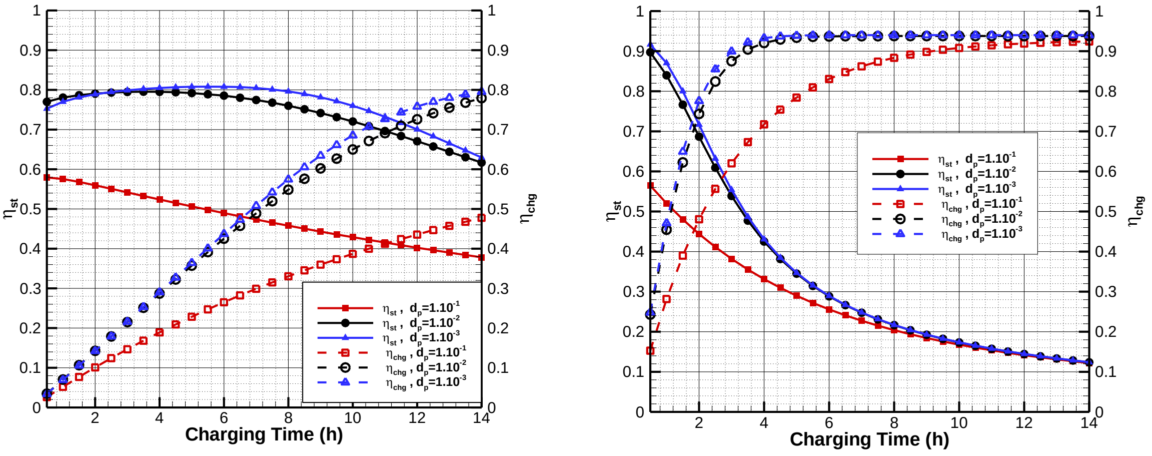

a) b)

Figure 7 Charge and storage efficiencies during the charge with different particle diameters, for: a)Re=1.10^4 b)Re=6.10^4

However, it is diifficult to compare the efficiency between the cases with different Re values if different hydrodynamic properties are considered. Nonetheless, in Fig. 9 and Fig. 10, the storage efficiency curves eventually cross the charging efficiency curves and this intersection represent the point in which the system has been charged a certain amount at a minimum storage efficiency of the same amount, for example if the curves intersect at 0.7 it follows that the system reached a 70% charge with at least 70% of storage efficiency. Here, this value is called thermal charge efficiency or η_{th} and is defined when η_{st} is equal to η_{chg} at a point in time t* in Fig. 9 and Fig. 10, as:

$$\eta_{th} = \eta_{st}(t^*) = \eta_{chg}(t^*) \quad (38)$$

Figure. 8 represents the value of η_{th} for all cases simulated. However, instead of using the values of particle diameter and porosity the efficiency is evaluated for different values of Re with respect to the Darcy number obtained by eqs. (31) and (32). Here, the decrease in the value of Da seem to effect an improvement in the thermal charge efficiency of the system for almost all of the cases. Since, the characteristic length is the same for all cases, lower Darcy numbers mean translate into lower permeabilities. Therefore, reducing the permeability of the system has a positive effect on the thermal charge efficiency for most of the cases herein. For Reynolds numbers, the thermal charge efficiency generally increases from 1.10^4 to 3.10^4 and then decreases with further increasing of Re numbers.

The highest η_{th} efficiency was achieved by the case with 0.8 porosity, with $d_p=1.10^{-3}$ m (translating to a value of $Da=1.10^{-9}$) and Re=30000, this case charged 77,5% of the total heat capacity of the solid filler with at least 77,5% of storage efficiency.

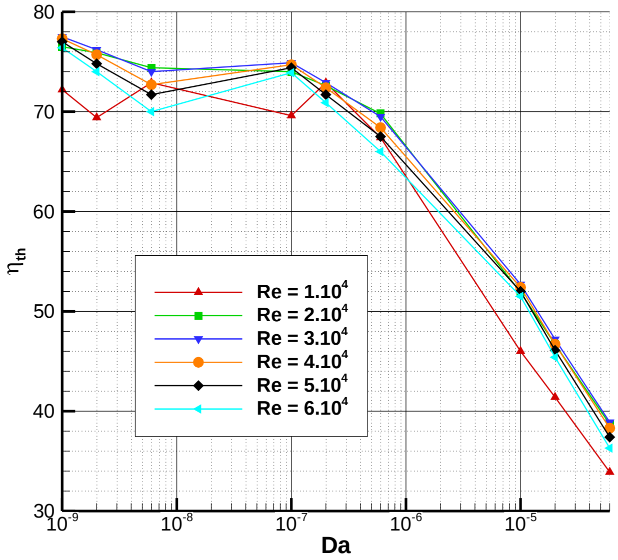

Figure 8. Overall thermal charge efficiencies η_{th} for different Re and Da numbers.

4 Conclusions

This study used a numerical model to examine the effect of the hydrodynamic properties of porosity and particle diameter on the charging cycle of a thermocline thermal energy storage tank.

A transient macroscopic two-energy equation model with k-ε turbulent flow model over a hybrid medium (porous and clear medium) was used to simulate hot air flow through a porous solid material. Using this model, it was possible to evaluate the thermal behavior throughout a charging cycle of a tank for porosities of 0.8, 0.85 and 0.9 and particle diameters of $d_p=1.10^{-1}$ m , $d_p=1.10^{-2}$ m and $d_p=1.10^{-3}$ m for Reynolds values from $Re=1.10^4$ to $Re=6.10^4$.

To observe the thermal behavior, transient temperatures were studied together with the storage and charge efficiencies. It was concluded that lower porosities are more efficient in storing heat. Additionally, smaller particle diameters allowed for more efficient heat exchange.

Finally, using the efficiency curves it was possible to define a thermal charge efficiency that provides an overall comparison between all the cases. This comparison corroborated the previous trends, showing that the most efficient charges were the ones with lower porosity and particle diameters which translates into lower values of Da. In addition, this implies that lower permeabilities are preferable for the range of TES systems here investigated. Moreover, increasing Re values increase the thermal charge efficiency up to a point and from then on, the results are of a slight diminishing in thermal charging efficiency with increasing Re.

Acknowledgements

The authors are thankful to CAPES, Brazil, for their invaluable support during the course of this research.

References

[1] EPE, “Projeção da demanda de energia elétrica para os próximos 10 anos (2015-2024),” Rio de Janeiro, 2015.

[2] X. Py, Y. Azoumah, and R. Olives, “Concentrated solar power: Current technologies, major innovative issues and applicability to West African countries,” *Renew. Sustain. Energy Rev.*, vol. 18, pp. 306–315, 2013.

[3] International Energy Agency, “Solar (PV and CSP),” 2016. [Online]. Available: http://www.iea.org/topics/renewables/subtopics/solar/. [Accessed: 14-Dec-2016].

[4] B. Xu, P. Li, and C. Chan, “Application of phase change materials for thermal energy storage in concentrated solar thermal power plants : A review to recent developments,” vol. 160, pp. 286–307, 2015.

[5] Pilkington Solar International GmbH, “Survey of Thermal Storage for Parabolic Trough Power Plants Period of Performance : Survey of Thermal Storage for Parabolic Trough Power Plants Period of Performance,” *NREL*, no. September, p. 61, 2000.

[6] M. B. Saito and M. J. S. de Lemos, “A macroscopic two-energy equation model for turbulent flow and heat transfer in highly porous media,” *Int. J. Heat Mass Transf.*, vol. 53, no. 11–12, pp. 2424–2433, 2010.

[7] M. H. J. Pedras and M. J. S. de Lemos, “Macroscopic turbulence modeling for incompressible flow through undeformable porous media,” *Int. J. Heat Mass Transf.*, vol. 44, no. 6, pp. 1081–1093, 2001.

[8] N. B. Santos and M. J. S. de Lemos, “Flow and Heat Transfer in a Parallel-Plate Channel with Porous and Solid Baffles,” *Numer. Heat Transf. Part A Appl.*, vol. 49, no. 5, pp. 471–494, 2006.

[9] F. D. Rocamora and M. J. S. de Lemos, “Analysis of convective heat transfer for turbulent flow in saturated porous media,” *Int. Commun. Heat Mass Transf.*, vol. 27, no. 6, pp. 825–834, Aug. 2000.

[10] E. J. Braga and M. J. S. De Lemos, “Turbulent natural convection in a porous square cavity computed with a macroscopic κ-ε model,” *Int. J. Heat Mass Transf.*, vol. 47, no. 26, pp. 5639–5650, 2004.

[11] M. J. S. de Lemos, *Turbulence in Porous Media: Modeling and Applications*, Second Edi. Elsevier Ltd, 2012.

[12] M. H. J. Pedras and M. J. S. de Lemos, “On the definition of turbulent kinetic energy for flow in porous media,” *International Communications in Heat and Mass Transfer*, vol. 27, no. 2. pp. 211–220, 2000.

[13] M. H. J. Pedras and M. J. S. de Lemos, “Simulation of Turbulent Flow in Porous Media Using a Spatially Periodic Array and a Low Re Two-Equation Closure,” *Numer. Heat Transf.*, vol. 39, no. 1, pp. 35–59, 2001.

[14] M. H. J. Pedras and M. J. S. de Lemos, “Computation of turbulent flow in porous media a low-Reynolds k-e model and an infinite array of transversally displaced elliptic rods,” *Numer. Heat Transf. Part A.*, vol. 43, no. 6, pp. 585–602, 2003.

[15] W. G. Gray and P. C. Y. Lee, “On the theorems for local volume averaging of multiphase systems,” *Int. J. Multiph. Flow*, vol. 3, no. 4, pp. 333–340, 1977.

[16] S. Patankar, “Numerical heat transfer and fluid flow,” *Series in coputational methods in mechanics and thermal sciences*. pp. 1–197, 1980.

[17] A. Mawire and M. McPherson, “Experimental and simulated temperature distribution of an oil-pebble bed thermal energy storage system with a variable heat source,” *Appl. Therm. Eng.*, vol. 29, no. 5–6, pp. 1086–1095, 2009.